

Surface Energy-Controlled SERS Substrates for Molecular Concentration at Plasmonic Nanogaps

Sung-Gyu Park,* ChaeWon Mun, Xiaofei Xiao, Avi Braun, Sunho Kim, Vincenzo Giannini, Stefan A. Maier,* and Dong-Ho Kim*

Positioning probe molecules at electromagnetic hot spots with nanometer precision is required to achieve highly sensitive and reproducible surface-enhanced Raman spectroscopy (SERS) analysis. In this article, molecular positioning at plasmonic nanogaps is reported using a high aspect ratio (HAR) plasmonic nanopillar array with a controlled surface energy. A large-area HAR plasmonic nanopillar array is generated using a nanolithography-free simple process involving Ar plasma treatment applied to a smooth polymer surface and the subsequent evaporation of metal onto the polymer nanopillars. The surface energy can be precisely controlled through the selective removal of an adsorbed self-assembled monolayer of low surface-energy molecules prepared on the plasmonic nanopillars. This process can be used to tune the surface energy and provide a superhydrophobic surface with a water contact angle of 165.8° on the one hand or a hydrophilic surface with a water contact angle of 40.0° on the other. The highly tunable surface wettability is employed to systematically investigate the effects of the surface energy on the capillary-force-induced clustering among the HAR plasmonic nanopillars as well as on molecular concentration at the collapsed nanogaps present at the tops of the clustered nanopillars.

1. Introduction

Plasmonic nanostructures enable light concentration, orders-of-magnitude higher than the incident light intensity, within the vicinity of tiny nanoscale gaps (so-called “hot spots”). Plasmonic enhancement via coupled localized surface plasmon resonance results in a high molecular detection sensitivity;^[1–7]

however, positioning probe molecules within the nanometer-scale volume of a hot spot tends to be difficult, resulting in poor reproducibility and controllability among surface-enhanced Raman spectroscopy (SERS) measurements. Therefore, controlling hot spot design and concentrating probe molecules at plasmonic nanogaps remains a goal for ultrasensitive and reproducible SERS detection. The most common method for localizing probe molecules at hot spots involves the use of nonwetable superhydrophobic plasmonic nanostructures.^[8–11] In the case of superhydrophobic (“Cassie–Baxter state”) nonwetable SERS nanostructures, probe molecules in a liquid drop become concentrated as the liquid evaporates, and the molecules are finally deposited on the top surface, where the hot spots are located. Through this approach, SERS nanostructures can significantly improve the SERS intensity of the probe molecules and enable ultrasensitive SERS detection.


Further, the development of plasmonic nanostructures with antibody-, enzyme-, or chemical ligand-functionalized surfaces would achieve molecular selectivity. This type of chemical treatment would involve capturing one specific target molecule through antibody–antigen or ligand–receptor binding interactions. For example, chemically modified Ag nanoparticles (NPs) with a self-assembled monolayer (SAM) of alkanethioates showed reversible binding affinity for glucose.^[12] In comparison to the bare Ag surfaces, which showed a very weak binding affinity to the glucose molecules, glucose was selectively partitioned into a SAM-modified Ag surface in the presence of an interfering protein (bovine serum albumin).^[13]

Physically trapping probe molecules at hot spots involve the use of capillary force-induced clustering among high aspect ratio (HAR) plasmonic nanopillars. This method relies primarily on solvent wetting (“Wenzel state”) to provide attractive capillary forces among HAR plasmonic nanopillars. As the liquid evaporates from the HAR plasmonic nanopillars, the HAR nanopillars bend and cluster together while probe molecules dissolved in the liquid can become trapped among the nanogaps formed at the tops of the clustered plasmonic nanopillars;^[14–19] however, under Wenzel state wetting, solution drops can spread in the horizontal direction while also penetrating vertically to the bases of the HAR nanopillars. Vertical spreading results in the

Dr. S.-G. Park, C. W. Mun, S. Kim, Dr. D.-H. Kim
Advanced Functional Thin Films Department
Korea Institute of Materials Science (KIMS)
Changwon, Gyeongnam 641-831, South Korea
E-mail: sgpark@kims.re.kr; dhkim2@kims.re.kr

X. Xiao, Dr. A. Braun, Dr. V. Giannini, Prof. S. A. Maier
The Blackett Laboratory
Department of Physics
Imperial College London
London SW7 2AZ, UK
E-mail: s.maier@imperial.ac.uk

Dr. V. Giannini
Instituto de Estructura de la Materia (IEM-CSIC)
Madrid 28006, Spain

 The ORCID identification number(s) for the author(s) of this article can be found under <https://doi.org/10.1002/adfm.201703376>.

DOI: 10.1002/adfm.201703376

random adsorption of molecules across the entire nanostructure surface (yielding an analyte dilution effect).^[14] Because the hot spots are highly localized only at nanogaps at the tops of the nanopillar clusters, a small number of molecules trapped at a hot spot can provide a moderate SERS intensity. Therefore, it is highly desirable to develop a new method for enriching probe molecules at collapsed nanogap region.

Here, we describe a strategy for achieving high molecular concentration at collapsed nanogaps using a surface energy-controlled HAR plasmonic nanopillar array. A large-area HAR plasmonic nanopillar array was generated using a simple nanolithography-free process consisting of Ar plasma treatment of a polyethylene terephthalate (PET) surface and subsequent Au evaporation onto the polymer nanopillars. This simple nanofabrication process has clear advantages compared to other nanolithographic processes, such as electron beam lithography or focused ion beam etching, in that it is cost-effective and enables the high-throughput production of large-area plasmonic substrates. The surface energy of the plasmonic nanostructures was controlled by the chemisorption of low surface-energy molecules (1H,1H,2H,2H-perfluorodecanethiol (PFDT)) onto the plasmonic nanopillar arrays and the selective removal of PFDT through Ar plasma treatment, resulting in the conversion of a superhydrophobic surface with a water contact angle (CA) of 165.8° to a hydrophilic state with a water CA of 40.0°, depending on the treatment time. The highly tunable surface wettability was used to systematically investigate the surface energy effects of the HAR plasmonic nanopillar array on the SERS intensity and the corresponding SERS sensitivity. Interestingly, hydrophobic plasmonic nanopillars with a wetted areal fraction of 50% exhibited both capillary-force-induced clustering of the HAR plasmonic nanopillars and molecular enrichment at the collapsed nanogaps. Unlike conventional superhydrophobic

SERS substrates, the water-repellent SERS substrates provided the lowest Raman intensity among the HAR plasmonic nanostructures tested here. We directly visualized the effects of the surface wettability on the self-clustering HAR plasmonic nanopillars and the localization of probe molecules after water evaporation. In the Cassie–Baxter state, the concentrated methylene blue (MB) molecules were mainly deposited at large interstitial sites (not hot spot regions); however, under optimized partial wetting conditions, molecular enrichment occurred mainly at self-limiting plasmonic nanogaps at the tops of the nanopillar clusters.

2. Results and Discussion

2.1. Nonlithographic Fabrication of Plasmonic Nanopillar Arrays

Maskless plasma treatment is a conventional method for producing large area polymer nanostructure arrays.^[20–23] In this work, we applied maskless Ar plasma treatments to a PET surface to generate a high areal density of polymer nanopillars (Figure 1a). Plasmonic nanostructures were then formed by thermally evaporating a 100 nm thick Au layer onto the polymer nanopillar layer. We achieved precise control over the aspect ratio and areal density of the plasmonic nanostructures by tuning the operating parameters of the Ar plasma treatment (Figure S1 of the Supporting Information). Finally, we applied a water droplet to the plasmonic nanopillar array to induce capillary force-driven self-clustering among the HAR plasmonic nanopillars.

Figure 1b shows a scanning electron microscopy (SEM) image of the as-prepared upright plasmonic nanopillar array after 5 min of Ar plasma treatment of the PET substrate and the

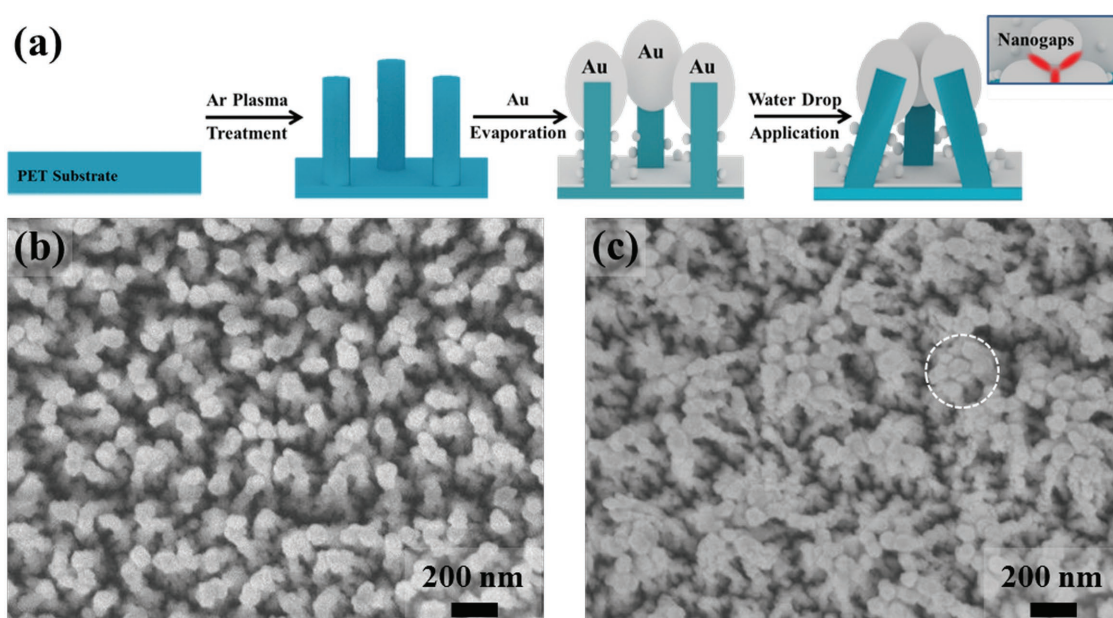


Figure 1. a) Schematic illustration of the fabrication of an Au/PET nanopillar array, and the capillary force-induced self-clustering of the plasmonic nanopillar array. The red area indicates a SERS hot spot at which a large local field enhancement occurred. SEM images of b) the upright as-prepared plasmonic nanopillar array, and c) the self-clustered plasmonic nanopillar array after water evaporation. The dotted circle highlights a cluster of size (N_c) 8.

subsequent evaporation of a 100 nm Au layer. The areal density of Au nanopillars was determined to be $31 \mu\text{m}^{-2}$ (Figure S2 of the Supporting Information), representing a 20–50% increase over the areal densities of previously reported plasmonic nanopillar arrays.^[14–16,19,24] PET has a low mechanical strength (Young's modulus of 2.76 GPa);^[25] therefore, the hybrid Au/PET nanopillars with an aspect ratio (AR) of 3 clustered together through capillary leaning effects (Figure S1 of the Supporting Information). The surface tension-driven leaning among the plasmonic nanopillars was initiated by introducing a small water droplet onto the plasmonic substrates. Water formed a CA of 40.7° on the HAR plasmonic nanopillar array, smaller than the CA of 64.0° obtained on the smooth Au thin film (Figure S3 of the Supporting Information). Because the water CA on the rough surface was smaller than that obtained on the smooth Au surface, our as-prepared plasmonic nanopillar array was present in a Wenzel state, and the liquid fully penetrated the interstices among the plasmonic nanopillars.^[26] Figure 1c shows an SEM image of the collapsed plasmonic nanopillar array after complete evaporation of a water droplet. The plasmonic nanopillars leaned together and clustered in a submicrometer area, and large crevices formed between the collapsed regions. The dotted circle indicates a nanopillar cluster of size (N_C) 8, defined as the number of aggregated nanopillars in a single cluster.

The key morphological features of the plasmonic nanopillar array were characterized by cross-sectional transmission electron microscopy (TEM) imaging, as shown in Figure 2a. The TEM image clearly shows a plasmonic nanopillar with an AR of 4, one large Au NP formed on top of the polymer nanopillar, and smaller Au NPs formed on the sidewalls. This characteristic morphology results from the directional deposition of Au during the thermal evaporation process and the nonwetting 3D growth of the NPs onto the PET surface.^[27] The TEM images also showed that lateral collapse dominated the high areal density arrays in which only a small degree of bending across the small interpillar distance was required for the nanopillars to adhere to one another. The outer nanopillars appeared to bend more than the inner nanopillars of a cluster. Lateral collapse resulted in top-clustered plasmonic nanopillars.

Figure 2b shows the finite-element simulation of the electric field distribution over the two leaning plasmonic nanopillars

with a nanogap size of 1 nm. Each plasmonic nanopillar was topped with one large prolate spheroid Au NP with an equatorial radius of 50 nm and a polar radius of 60 nm (similar to the Au NPs indicated by blue dotted lines in the TEM image). The Au NPs that formed on the sidewalls of the PET nanopillar were modeled as hemispheres with a radius of 10 nm. A linearly polarized 785.0 nm plane wave illumination beam was directed onto the plasmonic nanostructures with polarization along the dimer axis. Note that the region between the prolate spheroidal Au NPs at the top of the cluster showed the highest electric field enhancement, whereas Au NPs deposited onto the sidewalls of the PET nanopillar showed a decrease in the field enhancement toward the bottom of the PET nanopillar. The simulation results confirmed that the hot spot was highly localized at collapsed nanogaps on top of the Au NPs clusters. Therefore, positioning analyte molecules within the collapsed nanogap areas would ensure maximal SERS enhancement for ultrasensitive molecular detection. Ag is widely used for SERS and plasmonic applications due to its high quality factor across the entire visible wavelength range. However, it is highly sensitive to oxidation, which results in the poor stability. Au is suitable at longer wavelengths (more than ≈ 600 nm), and it also has good durability, biocompatibility, and high resistance to chemicals.^[1] Therefore Au is the most promising material for practical applications beyond ≈ 600 nm (in the red and near IR).

2.2. Precise Control over the Surface Energy of the Plasmonic Nanostructures

The roughness enhanced both the hydrophilicity and hydrophobicity of the array surfaces. In the Wenzel regime, surface roughness enhances the wettability of the hydrophilic nanostructures. In the Cassie–Baxter regime, air pockets should form below the liquid drop on the hydrophobic nanostructures, and trapped air pockets promote dewetting of the deposited liquids from the slippery surface, leading to superhydrophobicity.^[26,28] Because plasmonic nanostructured surfaces have a high roughness, we controlled the wettability by tuning the surface energy of the nanostructured surface. We showed that the as-prepared plasmonic nanostructures exhibited a Wenzel state (Figure S3 of the Supporting Information). The antiwetting

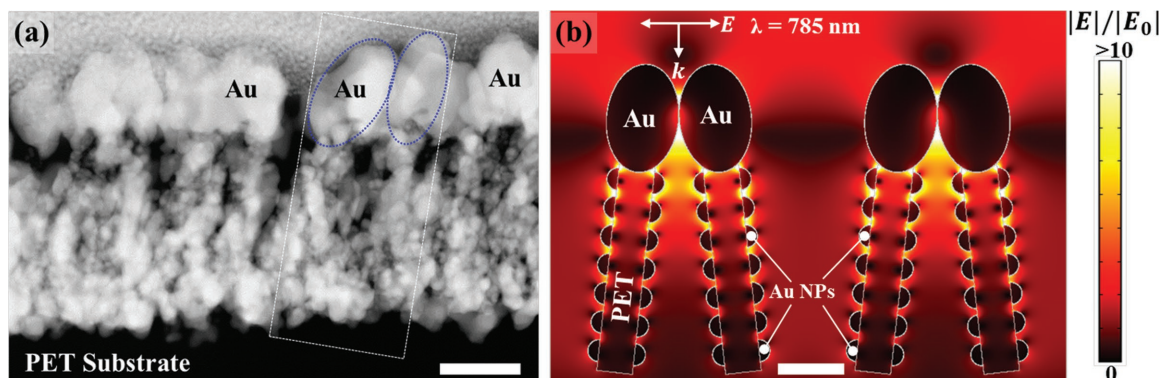


Figure 2. a) A TEM image of the clustered plasmonic nanopillars with an aspect ratio of 4. b) Finite-element simulation of the electric field distribution over the clustered plasmonic nanopillars with a gap size of 1 nm. A linearly polarized 785.0 nm plane wave illumination beam was directed onto the plasmonic nanostructures with polarization along the dimer axis. All scale bars were 100 nm.

properties of the plasmonic nanostructures were obtained from the specific chemisorption of PFDT molecules onto the Au surface. The thiol functional groups of the PFDT molecules were chemisorbed onto the Au film via strong thiolate–Au bonds, resulting in SAM of PFDT on the Au surface.^[29,30] The water CA (θ_w) on the fluorinated Au nanopillar array was 165.8°, whereas the water CA (θ_s) on the smooth fluorinated Au surface was 115.0° (Figure S4 of the Supporting Information). In the Cassie–Baxter state, the wetted areal fraction of the solid–liquid interface (f_{SL}) could be calculated as follows

$$\cos\theta_t = f_{SL}(1 + \cos\theta_s) - 1 \quad (1)$$

The value of f_{SL} was calculated to be 0.05, meaning that only about 5% of the surface area of the plasmonic nanopillars was wetted by water, and 95% of surface area was surrounded by air.

The low surface energy chemicals (i.e., PFDT in our case) adsorbed onto the plasmonic nanopillars were selectively removed by Ar plasma treatment. It is worth noting that the Ar plasma treatment process was applied under mild conditions, including a low plasma power and a short plasma treatment time, compared to the conditions used to generate the polymer nanopillar array. Figure 3 shows the changes in the water CAs as a function of the Ar plasma treatment time. The value of CA depended almost linearly on the plasma treatment time with a slope of -4° s^{-1} . These results indicated that we could precisely control the surface energy (thereby, the wettability) of the plasmonic nanostructures simply using Ar plasma treatment, because the PFDT molecules were removed from the top of the Au NPs prior to removal from the bottom of the Au nanostructures. The HAR plasmonic nanopillar array exhibited a Cassie–Baxter (CA > 150°) state until a plasma treatment time of 3 s (blue box in Figure 3), after which the array displayed hydrophobic properties and strong adhesion to water (i.e., partial wetting state, red box in Figure 3) at longer treatment times. After 10 s Ar plasma treatment, we obtained a HAR plasmonic nanopillar with a CA of 135.1° and resulting f_{SL} of 0.50. The

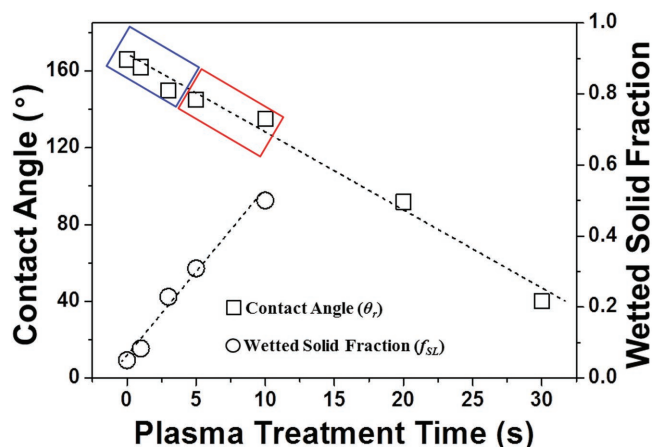


Figure 3. Tuning of the surface energy via selective removal of the chemisorbed perfluorodecanethiol molecules from the plasmonic nanopillar array. The blue and red boxes indicate the Cassie–Baxter state and hydrophobic partial wetting state, respectively. After 30 s Ar plasma treatment, the plasmonic nanostructures displayed a CA of 40.0°, restoring the original Wenzel wetting state with a CA of 40.7°.

wetted areal fraction ranged from 0.05 to 0.50 for the hydrophobic plasmonic nanostructures, depending on the plasma treatment time (black circles in Figure 3). After 30 s Ar plasma treatment, the plasmonic nanostructures were restored to a hydrophilic state (CA of 40.0°) due to the complete removal of PFDT. This surface was similar to that (CA = 40.7°) of the as-prepared nanopillar array.

2.3. Investigation of the Evaporation of Water Droplets from Plasmonic Nanostructures with Different Surface Energies

We studied the time-dependence of the water profile after applying an 8 μL water droplet onto the plasmonic nanopillar arrays with different surface energies (Figure 4a–c). The hydrophilic as-prepared HAR plasmonic nanopillar array without surface fluorination, characterized by an initial water CA of 40.7°, displayed a three-phase contact line that was strongly pinned during the evaporation process; therefore, the wetted area remained unchanged until complete evaporation (Figure 4a). The CA decreased rapidly with water evaporation, and the water evaporated completely within 1000 s (the inset of Figure 4d). We also investigated the water droplet profile on the HAR plasmonic nanopillar array prepared with an initial CA of 135.1° or a wetted areal fraction of 0.50 (Figure 4b and the inset of Figure 4d). Like the hydrophilic HAR plasmonic nanopillar array, the three-phase contact line was pinned upon droplet application and remained unchanged until complete evaporation (Figure 4b). The CA gradually decreased to 116.2° until 1800 s, after which the CA decreased rapidly until complete evaporation of water (Figure 4d). The superhydrophobic plasmonic nanopillar array exhibited a high CA exceeding 150.0° until 1800 s and remained above 136.6° until 5400 s (Figure 4c). The three-phase contact line was not pinned, and the contact area decreased during this period of time due to the highly slippery nature of superhydrophobicity. Air pockets trapped in the interstices of the fluorinated plasmonic nanopillar array produced a composite slippery solid–air–liquid interface (the inset of Figure 4d).^[28] This evaporation behavior from the superhydrophobic surface is typical of such systems and results in the analyte-concentration effect.^[8–10] As the CA decreased further (after 5400 s evaporation), a wetting transition from the Cassie–Baxter to the partial wetting state was observed with a pinned three-phase contact line. The CA suddenly fell upon additional water evaporation. Figure 4d presents the overall time-dependent CA of the water droplet deposited onto a HAR plasmonic array with different wettabilities. Distinct evaporation behaviors from the HAR plasmonic nanopillar arrays were observed for different surface energies.

2.4. Molecular Concentration at the Plasmonic Nanogaps Atop the Nanopillar Clusters

We investigated the effects of the surface wettability on the self-clustering HAR plasmonic nanopillars and the molecular enrichment at the collapsed nanogaps atop the clusters. An aqueous solution droplet of $15 \times 10^{-6} \text{ M}$ MB applied to the hydrophilic HAR plasmonic nanopillar array fully penetrated

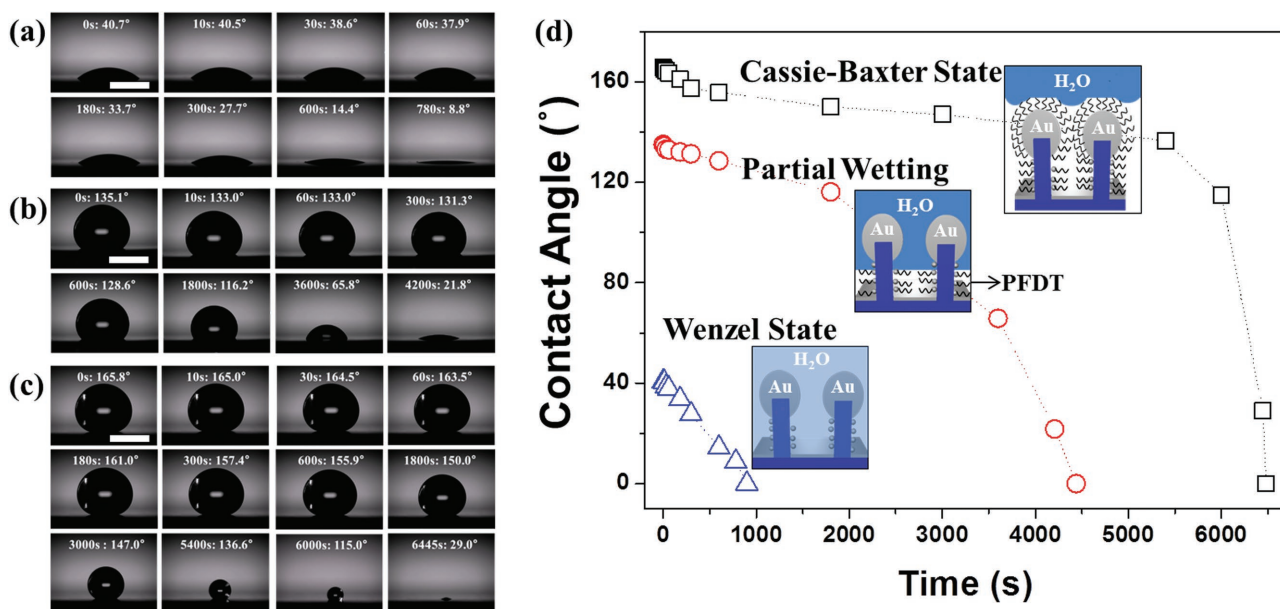


Figure 4. A series of images showing the drying of a water droplet on a plasmonic nanopillar array in a) the Wenzel state, b) the partial wetting state, or c) the Cassie–Baxter state. The scale bars in panels (a)–(c) indicate 2 mm. d) Time-dependent variations in the water contact angle on plasmonic nanopillar arrays prepared with different wetting conditions. The insets illustrate the degree of water wetting into the plasmonic nanopillars with different PFDT surface coverage levels (not drawn to scale).

the interstices among the plasmonic nanopillars. The water began to evaporate from the outmost air–liquid interface. The capillary meniscus interaction force among the liquid menisci surrounding the nanopillars then pulled the nanopillars and induced collapse into clusters,^[31,32] and a small number of MB molecules were trapped within the nanogaps at the tops of the clusters (Figure S5a of the Supporting Information). The collapsed HAR nanopillars remained surrounded by liquid, except at the tips. Therefore, most untrapped probe molecules remained dissolved and were concentrated as the water evaporated further, resulting in the uncontrolled random adsorption of probe molecules across the entire HAR nanopillar surface.^[14] In the HAR plasmonic nanopillar array with an f_{SL} of 0.50, the liquid penetrated top 50% of the surface area of the Au nanostructures, and the capillary meniscus interaction force acted on the plasmonic nanostructures as in a hydrophilic Wenzel state to form self-clustering nanogaps (Figure S5b of the Supporting Information). Because most of the MB molecules remained within the top 50% of the HAR plasmonic nanopillar surface during liquid evaporation, most MB molecules could be concentrated over the top 50% of the nanopillars. The re-entrant geometry of the fluorinated Au NPs deposited on the sidewalls of the PET nanopillars appeared to resist movement of the triple line along the vertical direction during water evaporation.^[33–35] We confirmed this MB deposition mechanism by comparing SEM images of the MB-deposited plasmonic nanopillar arrays. Only under partial wetting conditions with an f_{SL} of 0.50, clear MB deposits were located within the collapsed nanogaps atop the nanopillar clusters (Figure 5b and the dotted area in Figure 5e). Highly concentrated MB deposits were not observed in the case of the Wenzel state due to the analyte dilution effects (Figure 5a,d). In addition to the molecular concentration effects, we compared the cluster numbers obtained

from the various surface properties. The average N_c obtained under partial wetting conditions was 5, whereas N_c under Wenzel state conditions was 6 (Figure S6 of the Supporting Information). However, the number of bundled nanopillars increased to 61 over a $5 \times 4 \mu\text{m}^2$ area under partial wetting conditions, whereas 51 bundles were observed in the Wenzel state. Therefore, we concluded that under the optimized partial wetting conditions, we obtained collapsed nanogaps to provide strong near-field enhancement and molecular concentration at these hot spots. Since the capillary meniscus interaction force relied on the wetting of the tops of Au NPs on the flexible HAR polymer nanopillars, partial wetting conditions gave rise to an attractive force sufficiently strong to induce top clustering among the HAR nanopillars in the array.

The superhydrophobic HAR plasmonic nanostructures displayed a wetting transition from the Cassie–Baxter state to partial wetting conditions during the later stages of the evaporation process (Figure 4c). This transition could be understood in terms of the droplet droop model.^[36–38] The local deformation of a small droplet is governed by surface effects rather than by gravity. Since the curvature is the same at the top and bottom of a small droplet, the maximum droop of the droplet in the recessed region was located between two nanopillars. If the droop exceeded the depth of a nanopillar, the droplet contacted the bottom of the cavity between the pillars, resulting in a transition from the Cassie–Baxter state to a partial wetting state.^[36–38] Moreover, penetration of water vapor into the interstitial area may contribute to the observed phenomena during the later stages of the evaporation process.^[37] SEM images confirmed that large deposits of MB molecules mainly formed in the large interstitial areas among the nanopillars and the area surrounding the cluster perimeter (Figure 5c,f). These results indicated that the adhesive force of water in the recessed region

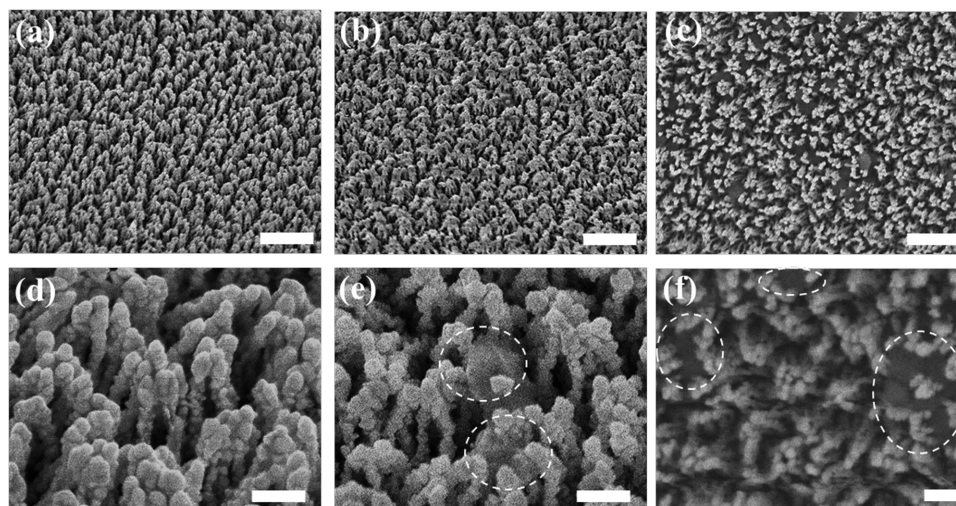


Figure 5. SEM images of an MB-deposited plasmonic nanopillar array after water evaporation in a,d) the Wenzel state, b,e) the partial wetting state, and c,f) the Cassie–Baxter state. The dotted circles in panel (e) indicate the MB molecules deposited in the nanogaps atop the nanopillar clusters, whereas the MB molecules in panels (c) and (f) were deposited mainly within the large interstitial areas among the nanopillars and the area surrounding the cluster perimeter (dotted region). The scale bars in panels (a)–(c) and (d)–(f) indicate 1 μm and 200 nm, respectively.

drove the deposition of highly concentrated MB molecules within the large interstitial area, and a repulsive force allowed the nearby nanopillars to push against the MB deposits (the dotted area of Figure 5f). This behavior was similar to that observed under high adhesive forces acting on colloidal nanoparticles deposited at defective sites in 3D holographically fabricated nanopillars.^[38]

2.5. The Effects of the Surface Energy on the SERS Performance

We designed a shadow mask pattern comprising a circular hole with a diameter of 3 mm and a period of 10 mm. A shadow mask $5 \times 5 \text{ cm}^2$ in size was then firmly attached to the smooth PET film during Ar plasma treatment and the subsequent Au evaporation process. After completing the fabrication process, the metal mask was detached from the substrate. The patterned plasmonic nanopillar arrays were useful for the SERS analysis of multiple samples on a single substrate^[39] or were cut into pieces for integration with a portable Raman spectrometer. **Figure 6a** shows a patterned large-area ($5 \times 5 \text{ cm}^2$) HAR plasmonic substrate with a pattern of 25 circles (detection points). Each circle enclosed a HAR plasmonic nanopillar cluster. Cutting lines at four corners provided single pieces of the SERS substrate. The pattern size could be significantly reduced by including a photolithography process in the fabrication process.^[39–41] The surface energies of the plasmonic nanostructures determined the wettability of the aqueous solution droplet containing probe molecules; therefore, we investigated the effects of the surface energy on the SERS performance, including the SERS intensity and limit of detection determination. The SERS substrate was integrated into a palm-sized Raman spectrometer for on-site SERS detection (Figure 6b). An aqueous solution droplet was applied to the center of the detection point of the SERS substrate, and the dried SERS substrate was mounted on the sample loading stage with the plasmonic nanopillars facing the incident laser.

Figure 6c presents a comparison of the MB SERS signals collected from the HAR plasmonic nanopillars under different wetting conditions at an excitation laser wavelength of $\lambda = 785.0 \text{ nm}$. Six microliters of aqueous solutions containing $15 \times 10^{-6} \text{ M}$ MB were dropped onto each SERS substrate. The SERS measurements were collected from the centers of the wetted areas of each substrate in order to avoid the coffee-ring effect.^[9] It should be noted that the HAR plasmonic nanopillar array prepared with an f_{SL} of 0.50 (i.e., Ar plasma treatment time of 10 s) exhibited superior SERS performances compared to the hydrophilic and superhydrophobic SERS substrates. The SERS signal enhancement measured under partial wetting conditions was 5.6 times the signal measured under hydrophilic conditions and 17.0 times the signal measured at the superhydrophobic SERS substrate. Because the MB molecules were highly concentrated outside of a hot spot region (Figure 5c,f), the superhydrophobic plasmonic nanopillar array exhibited the lowest SERS intensity observed here. Also, capping of the PFDT molecules prevented MB molecules from reaching the metal surface and reduced the SERS intensity because the SERS signal was dominated by the first layer of adsorbed molecules.^[18] At a lower concentration of $150 \times 10^{-9} \text{ M}$ MB, several Raman bands characteristic of MB were observed only under partial wetting conditions (Figure 6d). Given the detection area (a spot diameter of 25 μm) of a hand-held Raman spectroscopy, a $150 \times 10^{-9} \text{ M}$ MB solution produces a SERS signal at 0.10 fmol within a single field of view. It should be noted that partial wetting conditions yielded both the desired capillary force-induced leaning of the HAR plasmonic nanopillars and molecular concentration at the collapsed nanogaps.

3. Conclusions

In this work, we describe a method for positioning analyte molecules at a plasmonic nanogap through precise control over the surface energy of the high aspect ratio plasmonic nanopillar

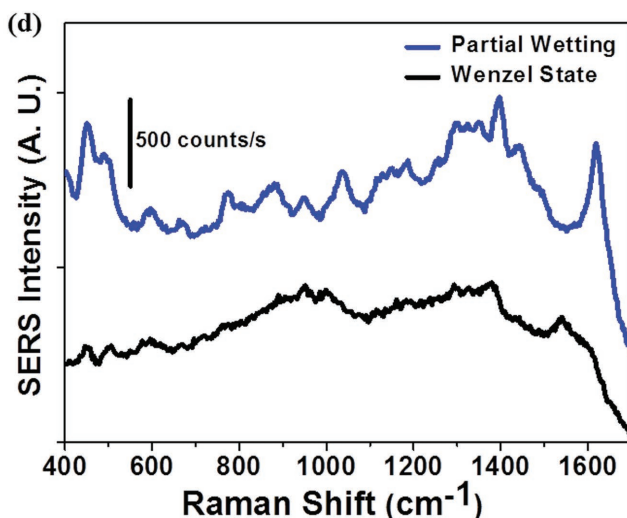
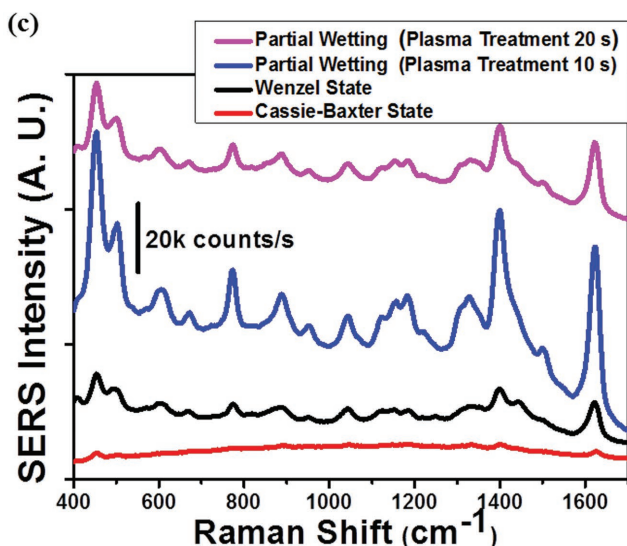
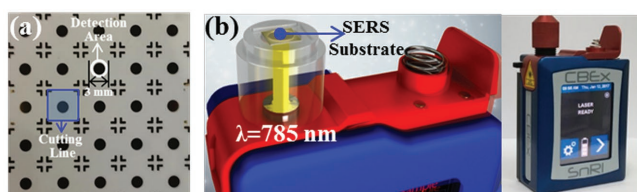


Figure 6. a) 5×5 SERS array over a large area (25 cm^2). b) Integration of the SERS substrate with a palm-size Raman spectrometer. The right-hand photograph shows a palm-size Raman spectrometer. Comparison of the SERS intensities of c) $15 \times 10^{-6} \text{ M}$ and d) $150 \times 10^{-9} \text{ M}$ methylene blue as a function of the wetting properties of the SERS substrate.

array. The surface energy was tuned via selective removal of the chemisorbed perfluorodecanethiol molecules from the plasmonic nanopillar array. Our approach generated high aspect ratio plasmonic nanopillars with a wetted areal fraction of 50%. Under these partial wetting conditions, we obtained both capillary force-induced self-clustering of plasmonic nanopillars as well as molecular enrichment at the plasmonic nanogaps atop the self-clustered nanopillars. Combining a portable Raman spectrometer with a low-cost but highly sensitive

SERS substrate, as demonstrated here, should enable practical SERS-based sensing applications, such as on-the-spot chemical detection and point-of-care medical diagnostics.

4. Experimental Section

Fabrication and Surface Fluorination of a High Aspect Ratio Gold Nanopillar Array: A PET polymer substrate with a thickness of $125 \mu\text{m}$ was purchased from Panac Inc. and was used without modification. PET pretreatment was performed using a custom-built 13.56 MHz radio frequency ion etching instrument (SNTEK, Co. Ltd). The inlet Ar flow rate and the working pressure were fixed, respectively, at 5 standard cubic centimeters per minute (sccm) and 80 mTorr during the pretreatment process. The plasma power was 100 W. Au nanostructures were directly grown on the PET nanopillars using a thermal evaporation system (SNTEK, Co. Ltd) with a deposition rate of 2.0 \AA s^{-1} , and a 100 nm thick Au film was deposited onto the PET nanopillars. The as-prepared Au nanostructures were then functionalized with PFDT. Specifically, $7 \mu\text{L}$ of a 97% PFDT solution were poured into a glass petri dish, and the lid of the petri dish was closed for 2 h. The lid was attached to the SERS substrates or a smooth 100 nm thick Au film. Selective removal of PFDT adsorbed onto the plasmonic nanostructures was performed using the same ion etching instrument. The etching process was operated under mild conditions to achieve the selective etching of chemicals. The inlet Ar flow rate and the working pressure were fixed, respectively, at 3 sccm and 80 mTorr during the pretreatment process. The plasma power was 50 W.

Characterizations: Water CAs were measured using CA goniometry (FEMTOFAB, SDLab-200TEZ). The surface morphologies were characterized by field emission scanning electron microscopy (FE-SEM; Jeol JSM-6700F). The SERS spectra were measured using a handheld Raman spectrometer (CBEx, Snowy Range Instruments) with a 785.0 nm laser. Laser power was 10 mW. The cross-sectional images of the plasmonic nanostructures were collected using TEM (Jeol JEM-2100 F).

Numerical Simulations: The numerical simulations were carried out using the COMSOL Multiphysics 5.1a. The structure was first sketched using Autodesk Fusion 360 and then imported into COMSOL Multiphysics. The linearly polarized 785.0 nm plane wave illumination beam was directed onto the plasmonic nanostructures with polarization along the dimer axis. In this calculation, the permittivity of gold was set to $\epsilon_{\text{Au}} = -22.855 + 1.425i$.^[42] The permittivity of PET was taken as 1.630.^[43]

Supporting Information

Supporting Information is available from the Wiley Online Library or from the author.

Acknowledgements

This study was supported financially by the Fundamental Research Program (PNK 5060) of the Korean Institute of Materials Science (KIMS). Dr. S.-G. Park is grateful for support from the Basic Science Research Program of the National Research Foundation of Korea (NRF), funded by the Ministry of Science, ICT and Future Planning (Grant No. NRF-2015R1C1A01053884). X. Xiao is grateful for support from the Lee Family Scholars. A.B. and S.A.M. acknowledge the EPSRC and ONR Global.

Conflict of Interest

The authors declare no conflict of interest.

Keywords

maskless plasma treatments, molecular concentration, plasmonic nanogaps, surface-enhanced Raman spectroscopy (SERS), surface energy

Received: June 20, 2017

Revised: July 26, 2017

Published online:

- [1] E. C. Le Ru, E. Blackie, M. Meyer, P. G. Etchegoin, *J. Phys. Chem. C* **2007**, *111*, 13794.
- [2] S. Nie, S. R. Emory, *Science* **1997**, *275*, 1102.
- [3] K. Kneipp, Y. Wang, H. Kneipp, L. T. Perelman, I. Itzkan, R. R. Dasari, M. S. Feld, *Phys. Rev. Lett.* **1997**, *78*, 1667.
- [4] J. Kneipp, H. Kneipp, K. Kneipp, *Chem. Soc. Rev.* **2008**, *37*, 1052.
- [5] W. Zhu, K. B. Crozier, *Nat. Commun.* **2014**, *5*, 5228.
- [6] R. Chikkaraddy, B. de Nijs, F. Benz, S. J. Barrow, O. A. Scherman, E. Rosta, A. Demetriadou, P. Fox, O. Hess, J. J. Baumberg, *Nature* **2016**, *535*, 127.
- [7] T. Y. Jeon, D. J. Kim, S.-G. Park, S.-H. Kim, D.-H. Kim, *Nano Convergence* **2016**, *3*, 1.
- [8] T. Y. Jeon, J. H. Kim, S. G. Park, J. D. Kwon, D. H. Kim, S. H. Kim, *Adv. Opt. Mater.* **2016**, *4*, 1893.
- [9] M. Lee, C. Mun, D.-H. Kim, S.-C. Chang, S.-G. Park, *RSC Adv.* **2016**, *6*, 92120.
- [10] X. Li, H. K. Lee, I. Y. Phang, C. K. Lee, X. Y. Ling, *Anal. Chem.* **2014**, *86*, 10437.
- [11] F. De Angelis, F. Gentile, F. Mecarini, G. Das, M. Moretti, P. Candeloro, M. L. Coluccio, G. Cojoc, A. Accardo, C. Liberale, R. P. Zaccaria, G. Perozziello, L. Tirinato, A. Toma, G. Cuda, R. Cingolani, E. Di Fabrizio, *Nat. Photonics* **2011**, *5*, 682.
- [12] M. D. Malinsky, K. L. Kelly, G. C. Schatz, R. P. Van Duyne, *J. Am. Chem. Soc.* **2001**, *123*, 1471.
- [13] C. R. Yonzon, C. L. Haynes, X. Zhang, J. T. Walsh, R. P. Van Duyne, *Anal. Chem.* **2004**, *76*, 78.
- [14] A. Kim, F. S. Ou, D. A. Ohlberg, M. Hu, R. S. Williams, Z. Li, *J. Am. Chem. Soc.* **2011**, *133*, 8234.
- [15] F. S. Ou, M. Hu, I. Naumov, A. Kim, W. Wu, A. M. Bratkovsky, X. Li, R. S. Williams, Z. Li, *Nano Lett.* **2011**, *11*, 2538.
- [16] M. S. Schmidt, J. Hübner, A. Boisen, *Adv. Mater.* **2012**, *24*, OP11.
- [17] J. L. Abell, J. D. Driskell, Y. Zhao, *Chem. Commun.* **2014**, *50*, 106.
- [18] H. Liu, Y. Sun, Z. Jin, L. Yang, J. Liu, *Chem. Sci.* **2013**, *4*, 3490.
- [19] M. Hu, F. S. Ou, W. Wu, I. Naumov, X. Li, A. M. Bratkovsky, R. S. Williams, Z. Li, *J. Am. Chem. Soc.* **2010**, *132*, 12820.
- [20] R. Di Mundo, M. Troia, F. Palumbo, M. Trotta, R. D'Agostino, *Plasma Processes Polym.* **2012**, *9*, 947.
- [21] T.-J. Ko, K. H. Oh, M.-W. Moon, *Adv. Mater. Interfaces* **2015**, *2*, 1400431.
- [22] J. Yun, W. Wang, S. M. Kim, T.-S. Bae, S. Lee, D. Kim, G.-H. Lee, H.-S. Lee, M. Song, *Energy Environ. Sci.* **2015**, *8*, 932.
- [23] J. Yun, T.-S. Bae, J.-D. Kwon, S. Lee, G.-H. Lee, *Nanoscale* **2012**, *4*, 7221.
- [24] N. U. L. Raman, M. S. Schmidt, A. Boisen, J. Ju, Q. Lin, *ACS Nano* **2013**, *7*, 5350.
- [25] Cambridge University Engineering Department, *Materials Data Book*, **2003**.
- [26] D. Quéré, *Annu. Rev. Mater. Res.* **2008**, *38*, 71.
- [27] C. T. Campbell, *Surf. Sci. Rep.* **1997**, *27*, 1.
- [28] S.-G. Park, S. Y. Lee, S. G. Jang, S.-M. Yang, *Langmuir* **2010**, *26*, 5295.
- [29] H. Häkkinen, *Nat. Chem.* **2012**, *4*, 443.
- [30] J. C. Love, L. A. Estroff, J. K. Kriebel, R. G. Nuzzo, G. M. Whitesides, *Chem. Rev.* **2005**, *105*, 1103.
- [31] D. Chandra, S. Yang, *Acc. Chem. Res.* **2010**, *43*, 1080.
- [32] D. Chandra, S. Yang, A. A. Soshinsky, R. J. Gambogi, *ACS Appl. Mater. Interfaces* **2009**, *1*, 1698.
- [33] T. L. Liu, C.-J. C. Kim, *Science* **2014**, *346*, 1096.
- [34] J. H. Kim, T. S. Shim, S. H. Kim, *Adv. Mater.* **2016**, *28*, 291.
- [35] A. Tuteja, W. Choi, M. Ma, J. M. Mabry, S. A. Mazzella, G. C. Rutledge, G. H. McKinley, R. E. Cohen, *Science* **2007**, *318*, 1618.
- [36] Y. C. Jung, B. Bhushan, *Scr. Mater.* **2007**, *57*, 1057.
- [37] X. Zhang, S. Tan, N. Zhao, X. Guo, X. Zhang, Y. Zhang, J. Xu, *Chem. Phys. Chem.* **2006**, *7*, 2067.
- [38] S.-G. Park, J. H. Moon, S.-K. Lee, J. Shim, S.-M. Yang, *Langmuir* **2010**, *26*, 1468.
- [39] T. Y. Jeon, S.-G. Park, D.-H. Kim, S.-H. Kim, *Adv. Funct. Mater.* **2015**, *25*, 4681.
- [40] S.-K. Lee, S.-G. Park, J. H. Moon, S.-M. Yang, *Lab Chip* **2008**, *8*, 388.
- [41] S.-G. Park, S.-K. Lee, J. H. Moon, S.-M. Yang, *Lab Chip* **2009**, *9*, 3144.
- [42] P. B. Johnson, R. W. Christy, *Phys. Rev. B* **1972**, *6*, 4370.
- [43] M. Kechadi, L. Chaal, V. Vivier, B. Tribollet, J. Gamby, *Phys. Chem. Chem. Phys.* **2016**, *18*, 20583.